OPEN ACCESS

Exploring the Storage Mechanism of Alkali Ions in Non-Graphitic Hard Carbon Anodes

Journal of The Electrochemical Society, 2023 **170** 090538

Exploring the Storage Mechanism of Alkali Ions in Non-Graphitic Hard Carbon Anodes

Haeseong Jang,[1,2] Ivana Hasa,[1,3] Hyunchul Kim,[4] Yoon Hwa,[5] Young-Woon Byeon,[4] Robert Kostecki,[1,z] and Haegyeom Kim[4,z]

[1]*Energy Storage and Distributed Resources Division, Lawrence Berkeley National Laboratory, Berkeley, CA, United States of America*
[2]*Department of Advanced Materials Engineering, Chung-Ang University, Anseong, 17546, Republic of Korea*
[3]*WMG, The University of Warwick, Coventry, CV4 7AL, United Kingdom*
[4]*Materials Sciences Division, Lawrence Berkeley National Laboratory, Berkeley, CA, United States of America*
[5]*School of Electrical, Computer and Energy Engineering, Arizona State University, Tempe, Arizona, United States of America*

This study aims to develop high-capacity hard carbon anode materials for alkali-ion batteries by controlling the microstructures of non-graphitic hard carbon through an annealing protocol and investigating the effects on the alkali-ion storage mechanisms using physical, chemical, and electrochemical analytical techniques. The hard carbon materials were synthesized at temperatures ranging from 900 °C to 1600 °C. Those synthesized at 1100 °C with high surface area and abundant defects exhibited the highest reversible capacity in Li- and K-ion systems, with the storage dominated by surface-adsorption mechanisms. In contrast, the hard carbon compounds prepared at 1400 °C with numerous curve-featured pores delivered the highest reversible capacity in the Na-ion system, indicating that these pores are the preferred Na-ion storage sites, particularly in low-voltage plateau regions. This study provides a comprehensive understanding of the relationship between microstructures and alkali-ion storage mechanisms in non-graphitic hard carbon and highlights the importance of tailoring the microstructures of hard carbon to achieve high specific capacity for the desired alkali-ion species.

 [DOI: 10.1149/1945-7111/acf88b]

Manuscript submitted May 24, 2023; revised manuscript received September 1, 2023. Published September 25, 2023.

Supplementary material for this article is available online

Lithium ion batteries (LIBs) have attracted significant interest as energy storage systems for various electronic devices owing to their high energy density, long calendar life, and good rate capability since their commercialization in 1991.[1] However, the potential scarcity of lithium resources and rapidly increasing demand for energy storage systems has led researchers to search for alternative battery systems that rely on Earth-abundant resources. Sodium- and potassium-based systems have been extensively studied as alternative metal-ion batteries among various Earth-abundant resource-based rechargeable batteries[2] as their entrance into the market is expected to be relatively easier than that of other battery systems given their similar operation principles as LIBs.[3] The development of high-performance electrode active materials is essential to realize the commercialization of sodium-ion batteries (SIBs) and potassium-ion batteries (PIBs). Researchers have recently reported several high-performance cathode active materials, including oxides, organic and polyanionic compounds, for SIBs and PIBs.[4–8] For anode active materials, carbonaceous materials have been widely adopted in alkali-ion batteries as promising candidates.[9] In particular, non-graphitic hard carbon (HC) demonstrates good performance in alkali-ion batteries, and the synthesis of HC is relatively simple and affordable.[3,9–11] Non-graphitic HC can uniquely store and release Na ions reversibly with a high specific capacity (>200 mAh g^{-1}) and low voltage (<0.5 V), whereas ordered graphitic carbon can exhibit a limited specific capacity below 10 mAh g^{-1} in SIBs. Even at high temperature chemical reaction conditions, only high stages of NaC_x ($x \geqslant 42$) could be synthesized.[12,13] Non-graphitic HC anodes have also been studied for PIBs by several research groups to take advantage of their amorphous-like structural feature that could have smaller volume change upon K-ion storage and release than graphite.[14]

An insightful understanding of the relationship between the alkali-ion storage behaviors and HC structures is required to develop improved HC anode materials. In this respect, several research groups have investigated the alkali-ion storage mechanisms in non-graphitic HC materials; however, there exists debate on the proposed mechanisms. For example, the Dahn and Nagao groups suggested the "house of cards" structure model for the sodium and lithium insertion mechanisms in HC compounds.[15–17] In a recent study, Kei et al. reported that lithiation is driven by interlayer insertion into defective carbon planes, whereas sodiation relies on pseudometallic Na cluster formation in micropores and potassiation mainly involves intercalation into narrow interlayer spaces of graphitic carbon planes.[18] A pore-filling storage mechanism, where Na or K ion could be stored in pores in the low-voltage region, has also been proposed.[19] Au et al.[20] and Reddy et al.[21] also reported Na adsorption/insertion at sloped voltage region followed by pore-filling mechanisms at plateau regions. Therefore, several synthesis approaches, such as using a pore-forming agent, pre-oxidation, and high-temperature carbonization, have been adopted as pore-tuning methods to utilize the pore-filling mechanism of HC.[22–24] In contrast, Gomez-Martin et al.[25] and Escamilla-Perez et al.[26] claimed the Na intercalation mechanisms in non-graphitic HC at low voltage plateau regions.

Although significant advances have been made in understanding the alkali-ion storage mechanisms in non-graphitic HCs, it is still debatable how alkali ions are stored in HC. In particular, it remains unclear how the intrinsic properties of HCs activate the pore-filling or intercalation mechanisms, how Na ions are stored in HC, how the Na storage mechanisms are affected by the local structure, and how the storage of Na in HC is different from that of other alkali ions such as Li and K. To answer these questions, in this study, we control the curved features of carbon sheets to form pores through the annealing protocol and investigate the effects on the alkali-ion storage performance. Various techniques, including X-ray diffraction (XRD), Brunauer–Emmett–Teller (BET) analysis, small-angle

[z]E-mail: R_Kostecki@lbl.gov; haegyumkim@lbl.gov

X-ray scattering (SAXS) analysis, Raman spectroscopy, and transmission electron microscopy (TEM), characterized the structural evolution of non-graphitic HC during the heat treatment. Raman analysis provides details of the structural evolution such as the curved feature, and we correlate such structure evolutions and alkali-ion storage properties in non-graphitic HC. By doing so, we find that curved features greatly affect the Na-ion storage properties but not Li- and K-ion storage. These findings indicate that the ideal storage sites depend on the type of alkali ion, emphasizing the need for tailored engineering of the microstructure of non-graphitic HC to maximize the specific capacity for the desired alkali-ion species.

Experimental Methods

Synthesis of hard carbon.—HC materials were synthesized by two-step heat treatment, and cellulose (Sigma-Aldrich, Product number: C6288, description: Fibers (Medium)) was used as a starting material. The cellulose was first heated at 275 °C for 1 h in ambient air, followed by high-temperature heat treatment at varied temperatures from 900 °C to 1600 °C for 8 h under continuous Ar flow.

Structure characterization.—The crystal structures of the obtained materials were analyzed using XRD on a Rigaku Miniflex 600 with Cu Kα radiation. The BET surface area of the samples was calculated by nitrogen (N_2) gas adsorption/desorption isotherms measured using an adsorption analyzer (ASAP 2020, Micromeritics Instrument Corp., Norcross, GA, USA) at 77.0 K. Prior to the analysis, the samples were out-gassed under vacuum at 200 °C overnight. The dried sample weight was measured to calculate the specific area corresponding to the adsorbed amount of N_2. SAXS measurements were performed at beamline 12-ID-C of the Advanced Photon Source, Argonne National Laboratory. The energy of the X-ray beam was 25 keV (wavelength $\lambda = 0.4959$ Å), and two setups (small- and wide- angle X-ray scattering, SAXS and WAXS) were used in which the sample to charge-coupled device detector (MAR research, Hamburg) distance were adjusted to achieve scattering q values of $0.0003 < q < 0.893$ Å-1, where $q = (4\pi/\lambda)\sin\theta$ and 2θ is the scattering angle. The 2θ angles of all the diffraction patterns were converted to corresponding angles for $\lambda = 1.54$ Å for easy comparison with other published XRD data. Raman spectra were collected using a Raman microscope system (Horiba Jobin Yvon USA, Inc.) equipped with an Ar-ion laser (Lexel Laser TM) adjusted to 633 nm. The spectra were collected with a microscope objective (Olympus America Inc.), and the laser power (~10 mW) was controlled to prevent sample damage. The laser spot size at the sample was approximately 2 μm in diameter. SEM images were recorded on a dual-beam focused ion beam-scanning electron microscopy (SEM) system (FIB-SEM, FEI Helios UX). The hard carbon powders were placed on the typical SEM carbon tape to fix them on the stage. Transmission electron microscopy (TEM) images were acquired on an FEI TitanX 60–300 microscope at an acceleration voltage of 300 kV. The hard carbon powders were diluted in Isopropyl alcohol (99.5%, anhydrous, Sigma-Aldrich) and sonicated for good particle dispersion. The TEM samples were prepared by drop-casting the solution onto a standard 300 copper mesh TEM grid with lacey carbon support. The samples were loaded into an FEI dual-tilt holder. X-ray photoelectron (XPS) measurements were performed on a Thermo Scientific K-Alpha XPS System with a monochromatic Al Ka X-ray source in the Molecular Foundry at LBNL.

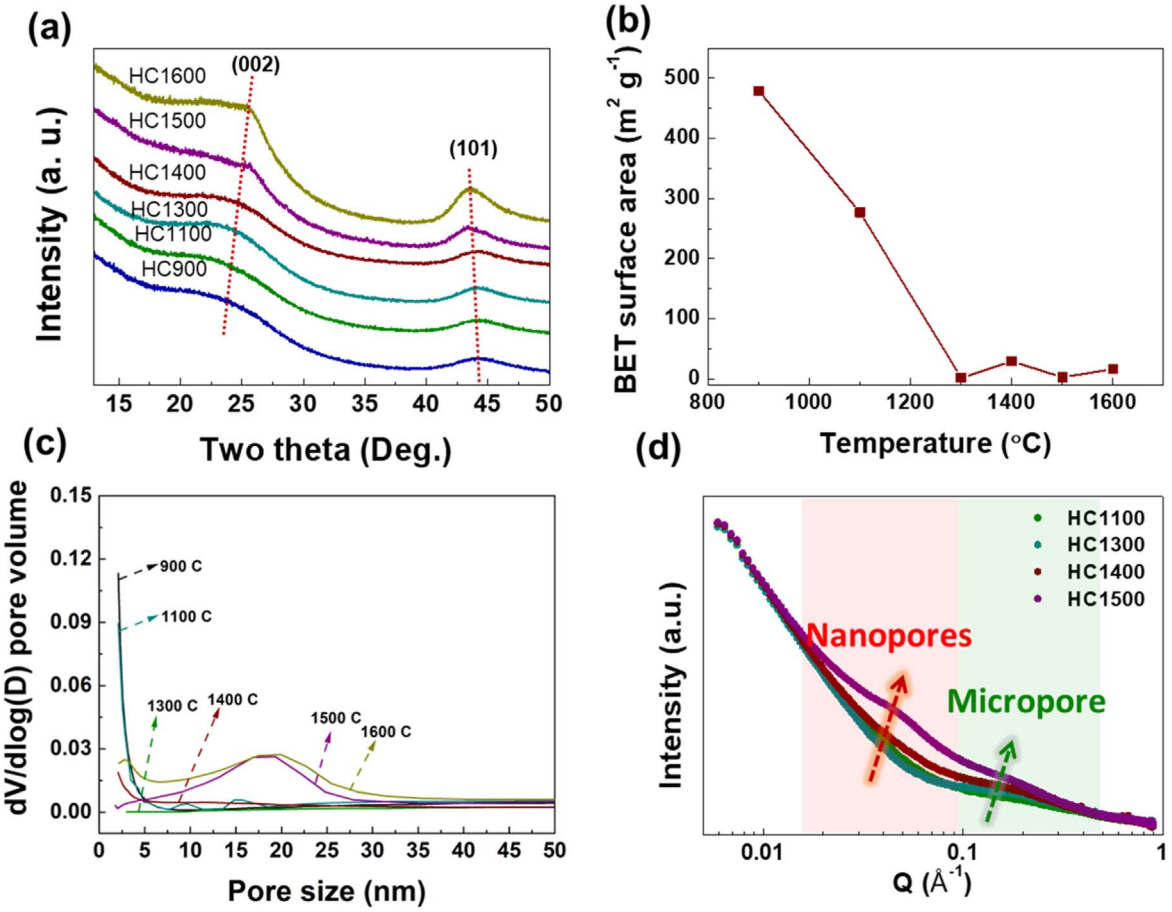

Figure 1. Structure evolutions of non-graphitic hard carbon upon heat treatment from 900 °C to 1600 °C. (a) XRD, (b) BET surface area, (c) Pore size distribution obtained from BET data, and (d) SAXS characterization results of non-graphitic hard carbon synthesized from cellulose.

Electrochemical test.—The electrodes were prepared by mixing the active material of HC (85 wt%), Super P carbon black (Timcal, 5 wt%), and sodium carboxymethylcellulose (Na-CMC, MW: 250,000, 10 wt%) binder with deionized water solvent. The slurry was pasted on Cu current collectors and dried in a 70 °C oven overnight. The test cells were assembled into 2032 coin-cells in a glove box with a two-electrode configuration using Li-, Na-, and K-metal counter electrodes. Electrolytes of 1 M $LiPF_6$, $NaPF_6$, and KPF_6 in ethylene carbonate/diethyl carbonate (EC/DEC, 1:1 vol ratio) were used for the Li, Na, and K cells respectively. A separator of grade GF/F (Whatman, USA) was used for all the cell tests. The electrochemical tests were performed using a battery testing station (BT-2000, Arbin Instruments).

Results

Structure evolutions of cellulose-derived hard carbons upon heat treatment.—HCs were synthesized from cellulose at varied pyrolysis temperatures (900 °C, 1100 °C 1300 °C, 1400 °C, 1500 °C, and 1600 °C) under continuous Ar flow, and the materials are denoted as HC900, HC1100, HC1300, HC1400, HC1500, and HC1600, respectively, hereafter. Figure 1a presents XRD patterns for all the HCs, with two broad peaks appearing at the diffraction angles of $2\theta = 22°–26°$ and $2\theta = 42°–46°$, representing the graphite planes of (002) and (101),[27,28] respectively. The (002) peak position gradually shifts to a higher angle with increasing pyrolysis temperature, which implies a decreased averaged lattice space along the *c*-axis. The interlayer distance of d(002), crystallite size along the *c*-axis (L_c) and *a*-axis (L_a) of the prepared samples, calculated from the fitting results (Fig. S1), are summarized in Table I. The sharper (002) and (101) peaks of HC1600 as compared with that of HC900 demonstrates that the local graphitic domains become larger at higher temperatures.

Nitrogen adsorption–desorption measurements were conducted to investigate the surface area of the prepared samples. Figure 1b shows the specific surface areas of HC samples calculated by the BET method. The BET surface areas of the prepared samples are summarized in Table I. We observed that the surface area of the HCs decreases significantly as the pyrolysis temperature changes from 900 °C to 1300 °C. At temperatures above 1300 °C, there is insignificant fluctuation in the surface area of the HCs, indicating that the loosely packed carbon structures are more ordered and densified at higher temperatures. Figure 1c shows the pore size distributions in HC samples, which were estimated by Barrett–Joyner–Halenda (BJH) model. It demonstrates that the pore size increases as the synthesis temperature increases.

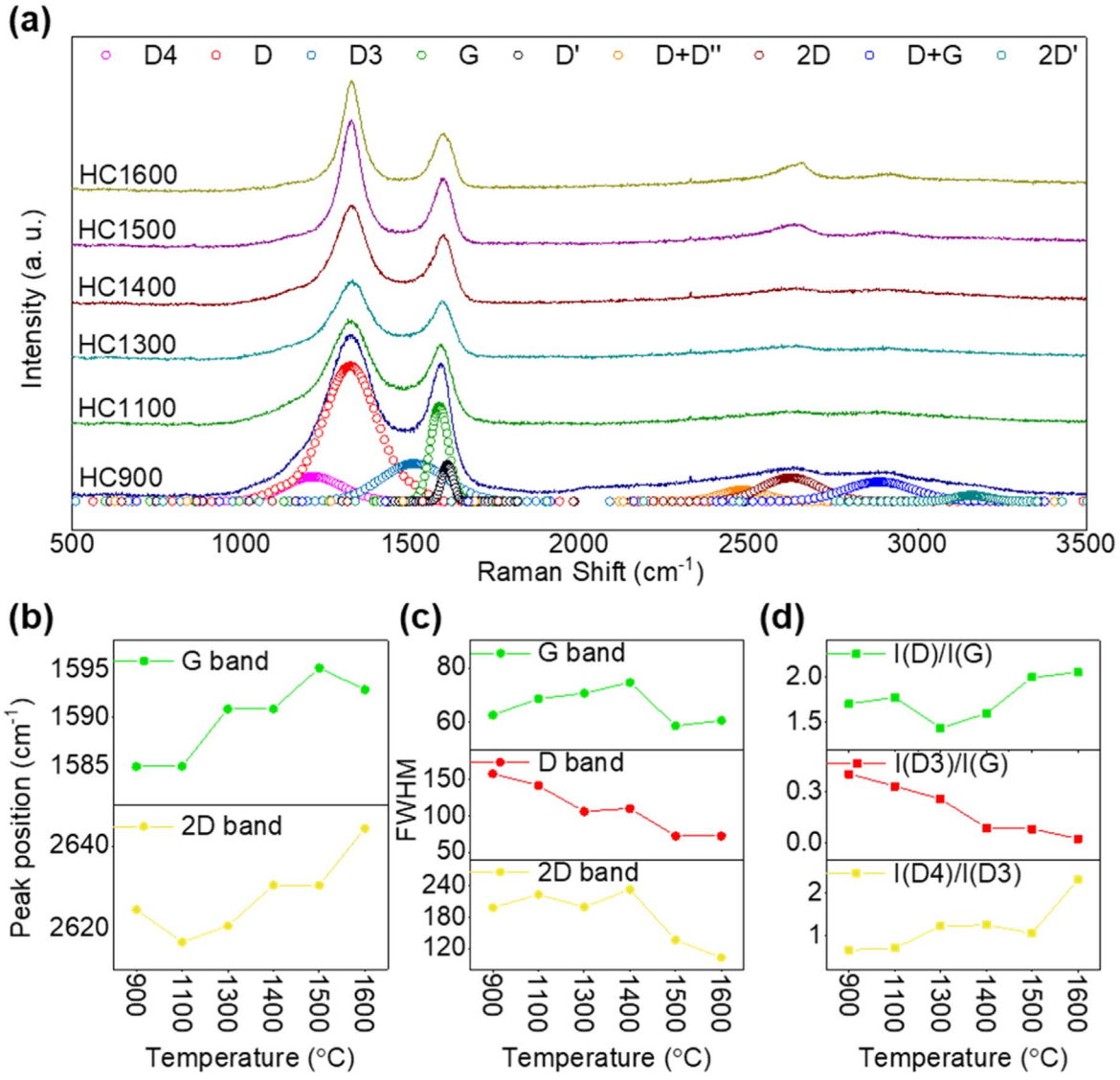

Figure 2. Raman spectra with 633-nm wavelength laser. (a) Raman spectra of prepared samples with proposed spectra deconvolution; (b) position change of 2D-, G-, and D-band peak; (c) FWHM change of 2D-, G-, and D-band peak; (d) intensity ratio change of D3/G, D4/D3, and D/G.

Table I. Calculated interlayer distance of d(002) and crystallite size along the *c*-axis (Lc) and *a*-axis (La) from fitting curves of XRD and BET surface area.

Sample	Interlayer distance (Å)	Crystallite size along *c*-axis (nm)	Crystallite size along a-axis (nm)	BET surface area ($m^2\ g^{-1}$)
HC 900	3.749	1.07	1.65	479
HC 1100	3.744	1.11	1.70	277
HC 1300	3.777	1.14	1.78	1.6
HC 1400	3.715	1.23	2.02	29.4
HC 1500	3.715	1.24	2.34	2.85
HC 1600	3.675	1.32	2.31	16.15

We employed the SAXS technique, where the energy of the X-ray beam was 25 keV (wavelength $\lambda = 0.4959$ Å), to evaluate the closed pores inside the HC matrix because BET technique is sensitive open pores at the surface only. Figure 1d represents the scattering intensity, which is a function of the electron density fluctuation, as a function of the scattering vector ($0.0003 < q < 0.893$ Å^{-1}, $q = (4\pi/\lambda)\sin\theta$ and 2θ is the scattering angle). The 2θ angles of all the diffraction patterns were converted to corresponding angles for $\lambda = 1.54$ Å for easy comparison with other published XRD data. The SAXS patterns of the prepared HC samples show two broad maxima: one between 0.02 and 0.1 Å, and the other between 0.1 and 0.5 Å, which arise from the nanopores and micropores in the carbon matrix, respectively.[28,29] The scattering intensity of the peaks increases with temperature, suggesting an increase in the electron-density contrast between the carbon matrix and closed pores.[30] This suggests that the total volume of closed pores increases in the HC structure as the synthesis temperature increases. Given that the BET surface area decreases with increasing temperature, the increase of the total closed pore volume might indicate that the open pores are transformed into closed pores in the non-graphitic HC because the high BET surface area usually comes from the open pores at the surface of carbon.

Raman spectroscopy was used to further characterize the fine structural information of the HCs, including the crystallinity, carbon-atom hybridization, defect concentrations, and ordering range.[31] Figure 2a presents the Raman spectra of the HC samples in the region from 500 to 3500 cm^{-1} obtained using a 633-nm wavelength laser. The first-order Raman spectrum of the HC samples could be deconvoluted into five components, including the D, G, D4, D3, and D' bands.[32,33] The D band, assigned to *K*-point phonons of A_{1g} symmetry, is related to the breathing modes of six-atom rings. The presence of the D band usually implies discontinuity of the sp^2 symmetry in carbon domains, which is associated with the edge effects, point defects and structural disorder. The G band, assigned to zone-center phonons of E_{2g} symmetry, is related to the in-plane bond stretching modes of all the sp^2 atoms in both carbon hexagonal rings. The D4 band, attributed to sp^2–sp^3 bonds, is related to C–H termination groups such as C=C/C–C stretching motions in a polyene-like structure.[34] The D3 band is related to the vibrational response of the amorphous carbon content and indicates the presence of amorphous domains in the structure.[32,35,36] The D' band is related to the graphitic lattice vibration mode of the surface graphene layers.[32,37] The second-order Raman spectrum could be deconvoluted into four components, including D+D′-, 2D-, D+G-, and 2D′ bands. All four components are related to overtones and combinations of known lattice fundamental vibration modes.[32] The fitting parameters of all the HC samples, which are the peak position, normalized intensity, FWHM, and area, are listed in Table S1.

To highlight the structure changes of HCs at varied heat-treatment temperatures, we plot the position and full width at half maximum (FWHM) changes of the 2D-, G-, and D-band peaks, as represented in Figs. 2b and 2c. We observed the continuous upshift of the G-band peak position, indicating that the sp^3 component decreases, whereas sp^2 component increases, with increasing treatment temperature. This observation points to the phase transformation from amorphous carbon to nanocrystalline graphite or a more ordered carbon structure upon heating.[33] Interestingly, the FWHM of the G-band peak increases from 900 °C to 1400 °C and then

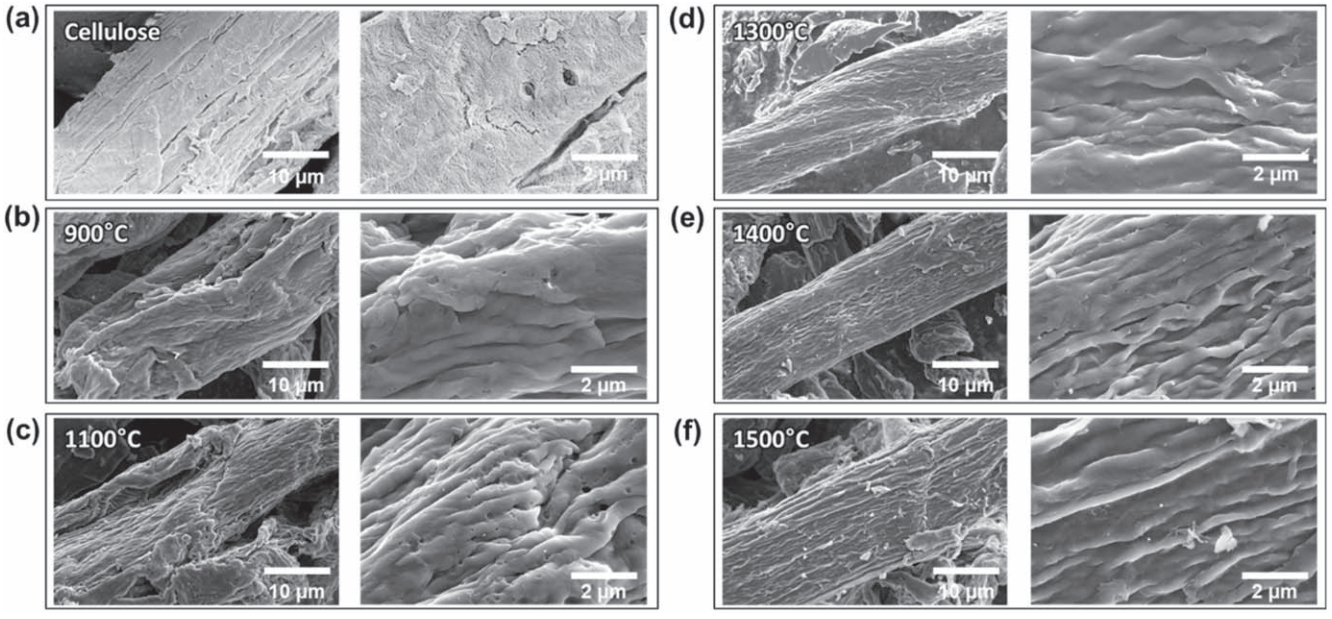

Figure 3. SEM images of cellulose, and HC samples synthesized at varied temperatures. SEM images of (a) cellulose, HC sample synthesized at (b) 900 °C, (c) 1100 °C, (d) 1300 °C, (e) 1400 °C, and (f) 1500 °C.

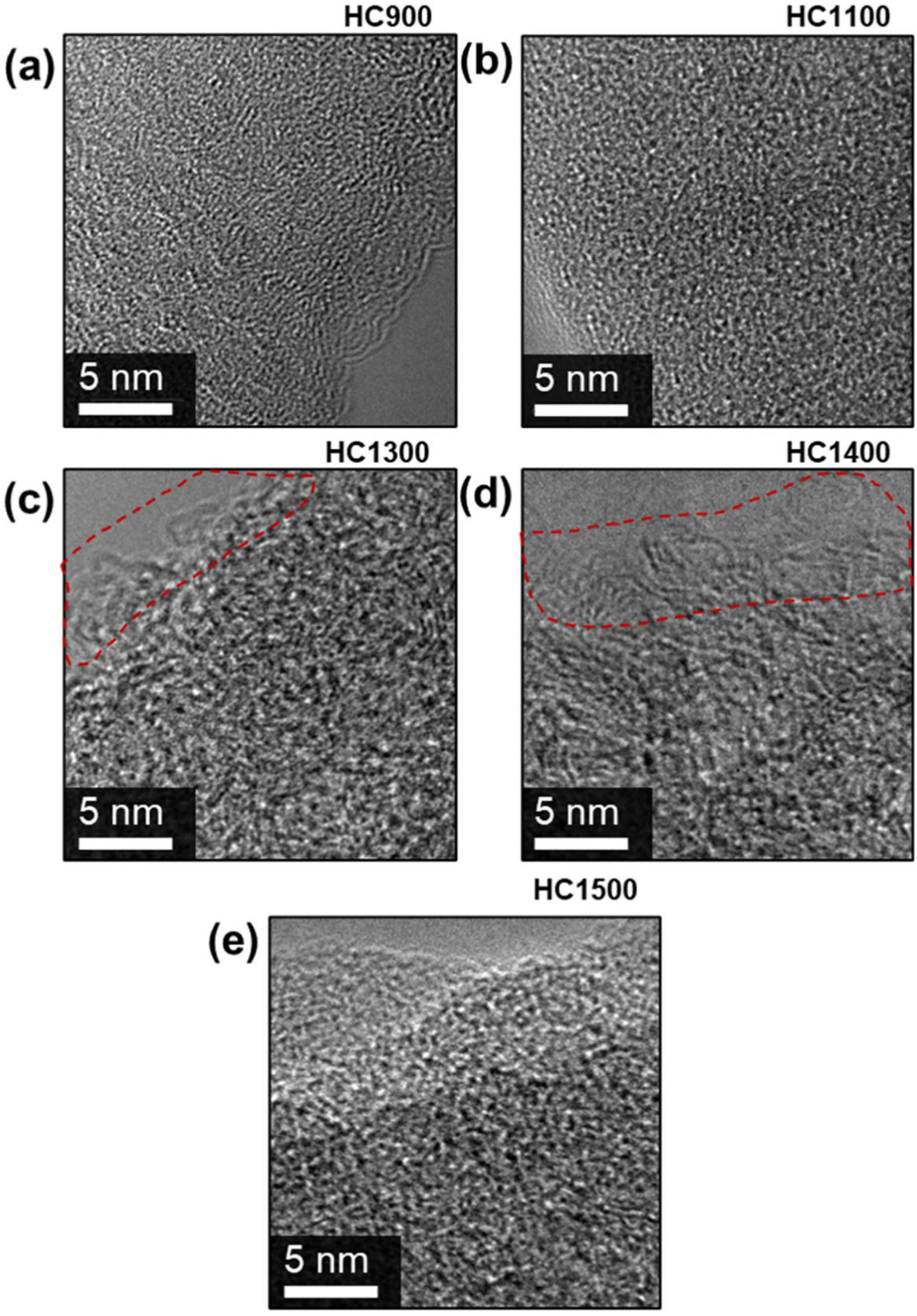

Figure 4. TEM images of HC samples synthesized at varied temperatures. TEM images of HC sample synthesized at (a) 900 °C, (b) 1100 °C, (c) 1300 °C, (d) 1400 °C, and (e) 1500 °C.

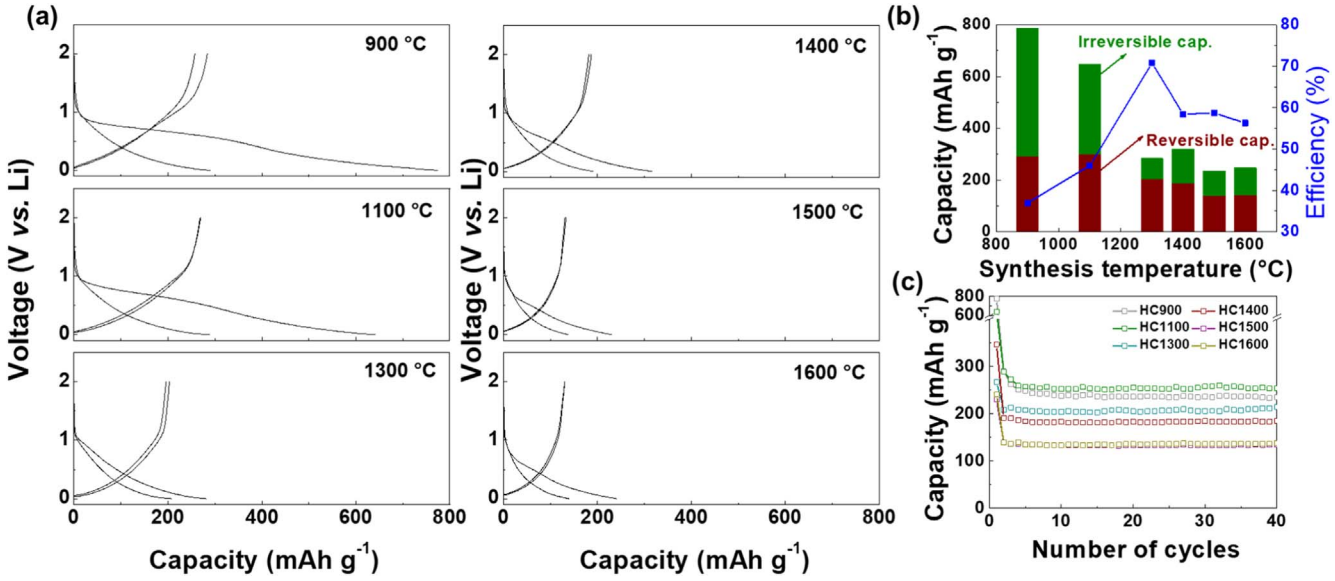

Figure 5. Electrochemical properties of non-graphitic hard carbon in Li cells. (a) Charge–discharge profiles, (b) capacity vs synthesis temperature plots, (c) cycling stability of HCs.

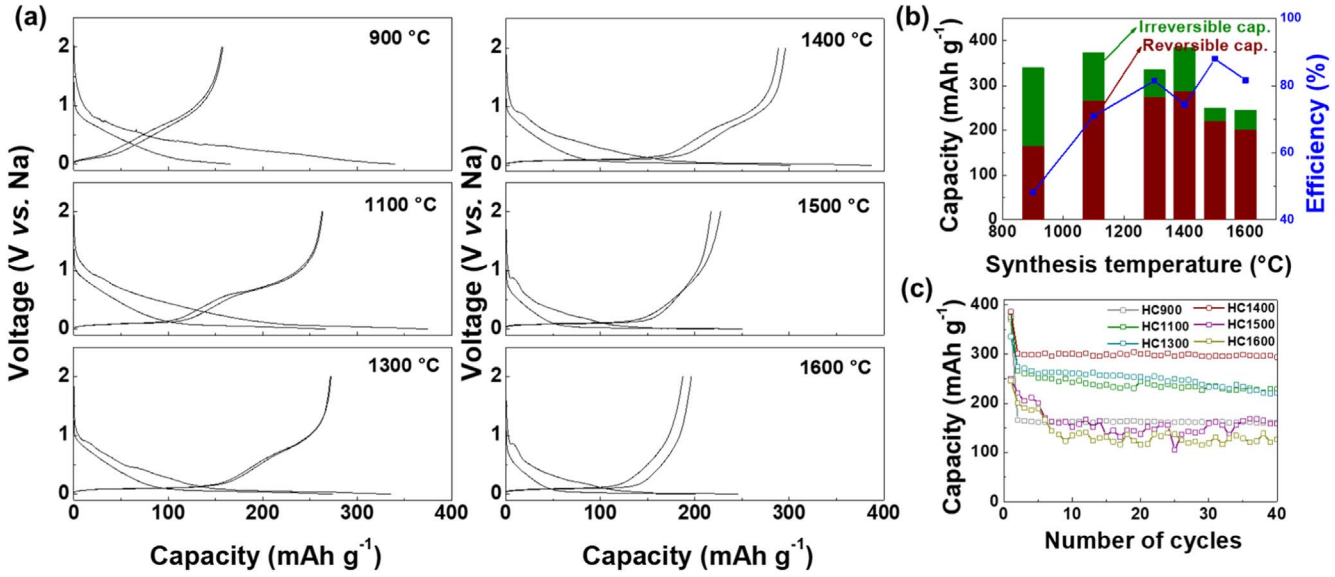

Figure 6. Electrochemical properties of non-graphitic HC in Na cells. (a) Charge–discharge profiles, (b) capacity vs synthesis temperature plots, (c) cycling stability of HCs.

decreases from 1400 °C to 1600 °C, which can be interpretated as the C–C bond length becoming more diversified until the heat-treatment temperature reaches 1400 °C and then unified at higher temperatures.[38] This finding might indicate that there exist some C5 and C7 rings and/or an incomplete C6 local structure with an open edge in the HC. We expect these defect components likely contribute to the formation of curvatures of HC materials,[39,40] and these curved features of non-graphitic HC form micro- and nanopores, as confirmed by the SAXS analysis (Fig. 1d). The gradual decrease of the FWHM of the D-band peak with increasing temperature indicates an enlarged graphitic basal plane.[41] The increase in the D-band peak intensity along with the decrease in the D'-band peak intensity (Fig. S2) could be attributed to structural defects such as edges with different chirality or vacancies.[42,43] The 2D-band peak is often used as an indicator of the stacking level of the graphene layers.[33,44] The shape of the 2D-band peak in Fig. 2a shows a symmetric feature, indicating that synthesized HCs have the Bernal stacking (ABA) rather than rhombohedral stacking (ABC).[45] The position, FWHM, and intensity change of the 2D-band peak strongly depend on the rotational angle of the graphene layers.[46] The observed continuous increase of the 2D-band peak intensity and variation in the 2D-band peak position and FWHM with increasing temperature in Fig. S2 and Figs. 2b, 2c could be attributed to the unconventionally stacked multi-layer graphene induced by an increase in the misorientation angle between layers.[46] Figure 2d shows the I(D)/I(G), I(D3)/I(G), and I(D4)/I(D3) ratio change. Interestingly, the I(D)/I(G) ratio does not change monotonically. The I(D)/I(G) ratio, which is often used to estimate the degree of graphitization,[40,47] decreases from 900 °C to 1300 °C and gradually increases above 1300 °C. This might indicate the structure evolution is not a simple process from amorphous to ordered structure. Because the I(D3)/I(G) and I(D4)/I(D3) ratios are indicators of the C–C bond angle disorderness,[32] we speculate that the reduction in the I(D3)/I(G) ratio and the rise in the I(D4)/I(D3) ratio indicate an increase of the C–C bond angle orderness in the turbostratic carbon with increasing synthesis temperature.[31,32] Given that the C–C bond

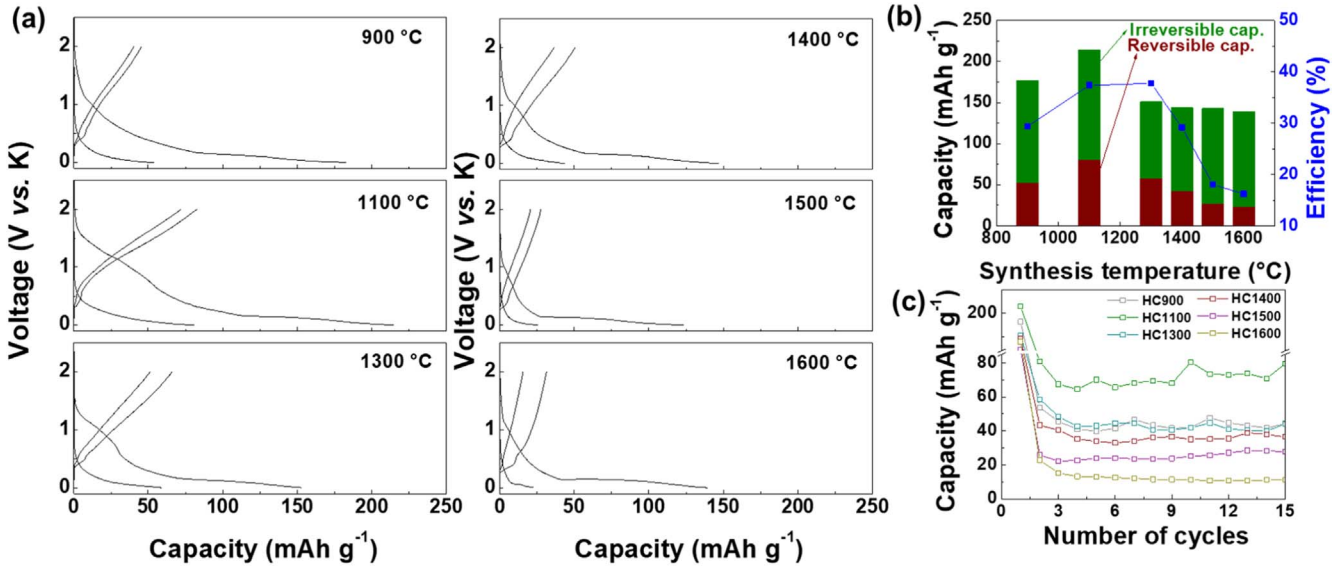

Figure 7. Electrochemical properties of non-graphitic HC in K cells. (a) Charge–discharge profiles, (b) capacity vs synthesis temperature plots, (c) cycling stability of HCs.

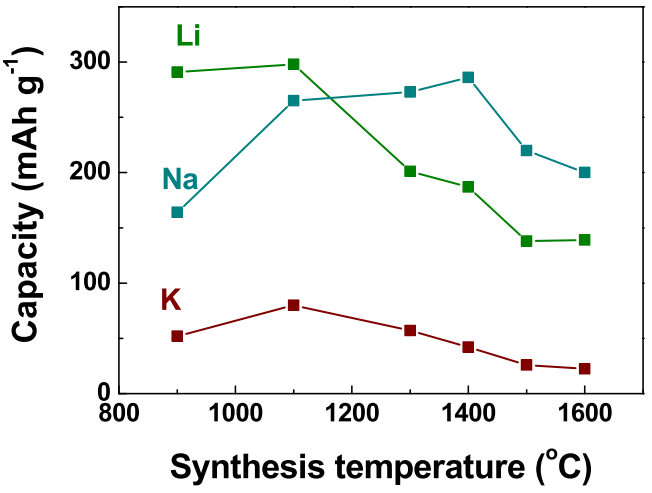

Figure 8. Synthesis temperature of HC vs reversible capacity in Li, Na, and K cells.

angle in a honeycomb structure becomes more ordered, the diversification of the C–C bond length by heat treatment up to 1400 °C, as observed from the change of the FWHM of the G-band peak in Fig. 2c, could be attributed to the incomplete formation of the C6 ring, in which one C–C bond edge is open, rather than C5 and C7 ring formations. With all these Raman spectra observations, we conclude that the structure evolution of HC compounds is not a simple transformation from disorderness to orderness as the temperature increases. Instead, we find that increasing the synthesis temperature up to 1400 °C induces the growth of graphitic basal planes and an increase of the C–C bond angle orderness yet increases structural disordering such as the growth of disordered carbon clusters and increased open edges, vacancies, and misorientation of the layers. Temperatures higher than 1400 °C lead to a more ordered structure of HCs overall.

From the comprehensive analysis using XRD, BET, SAXS, and Raman spectroscopy, the structural evolution of cellulose-derived HCs with elevated synthesis temperature can be categorized into three stages, leading from amorphous-like carbon to turbostratic carbon. Stage 1 (900 °C—1100 °C) consists of amorphous-dominant carbon, containing many defects, and high surface area. In stage 2 (1100 °C—1400 °C), the graphene sheets start to have the curved features and form micropores while the graphene sheets become aligned. In stage 3 (1400 °C—1600 °C), the interlayer distance between graphene sheets decreases and the C–C bond length is unified to form flattened and ordered nano-graphitic carbon. The microstructure still contains hierarchical porosity, including nanopores and micropores but much fewer curved features of the carbon sheets.

We further characterize morphology and microstructure evolutions of HC samples by heat treatment. Figure 3 shows the SEM images of cellulose, and HC samples synthesized at varied temperatures. We confirm that the fiber-like morphology of cellulose is maintained even at high temperature treatment up to 1500 °C while the surface becomes more wrinkled. Figure 4 exhibits TEM images of HC samples synthesized at varied temperatures from 900 °C to 1500 °C. For HC900 and HC1100 samples, we observed tiny domains that are randomly oriented (Figs. 4a–4b). Interestingly, we find curved fringes in HC1300 and HC1400 samples (Figs. 4c–4d), and these curved features of carbon sheets disappear in HC1500 sample (Fig. 4e). This behavior is more highlighted in the edge side of the carbon samples. For example, the edge of the HC900, HC1100, and HC1500 samples show relatively flattened features compared to HC1300 and HC1400 samples that exhibit heavily curved features (highlighted area in Figs. 4c–4d). These microstructure evolutions are in a good agreement with our interpretation from Raman analysis.

Electrochemical Li, Na, and K storage properties.—The electrochemical performance tests of cellulose-derived HCs were conducted in Li half cells to investigate the electrochemical characteristics of non-graphitic HCs as anodes for LIBs. Figure 5a shows the first and second charge–discharge profiles at a current rate of 15 mA g^{-1} in the voltage range of 0.001–2.0 V vs Li/Li^+. All of the cellulose-derived HCs show the plateau at approximately 0.9 V in the first discharge, with the plateau disappearing in the second discharge. The plateau at 0.9 V can likely be attributed to the irreversible solid-electrolyte interphase (SEI) layer formation.[48] In the first cycle, the reversible/irreversible capacity of HC900, HC1100, HC1300, HC1400, HC1500, and HC1600 are 291/496, 298/350, 201/83, 187/133, 138/97, and 139/108 mAh g^{-1}, corresponding to a low coulombic efficiency (CE) of 37.0%, 46.0%, 70.8%, 58.4%, 58.7%, and 56.3%, respectively. The large irreversible capacity of the first cycle can be ascribed to the decomposition

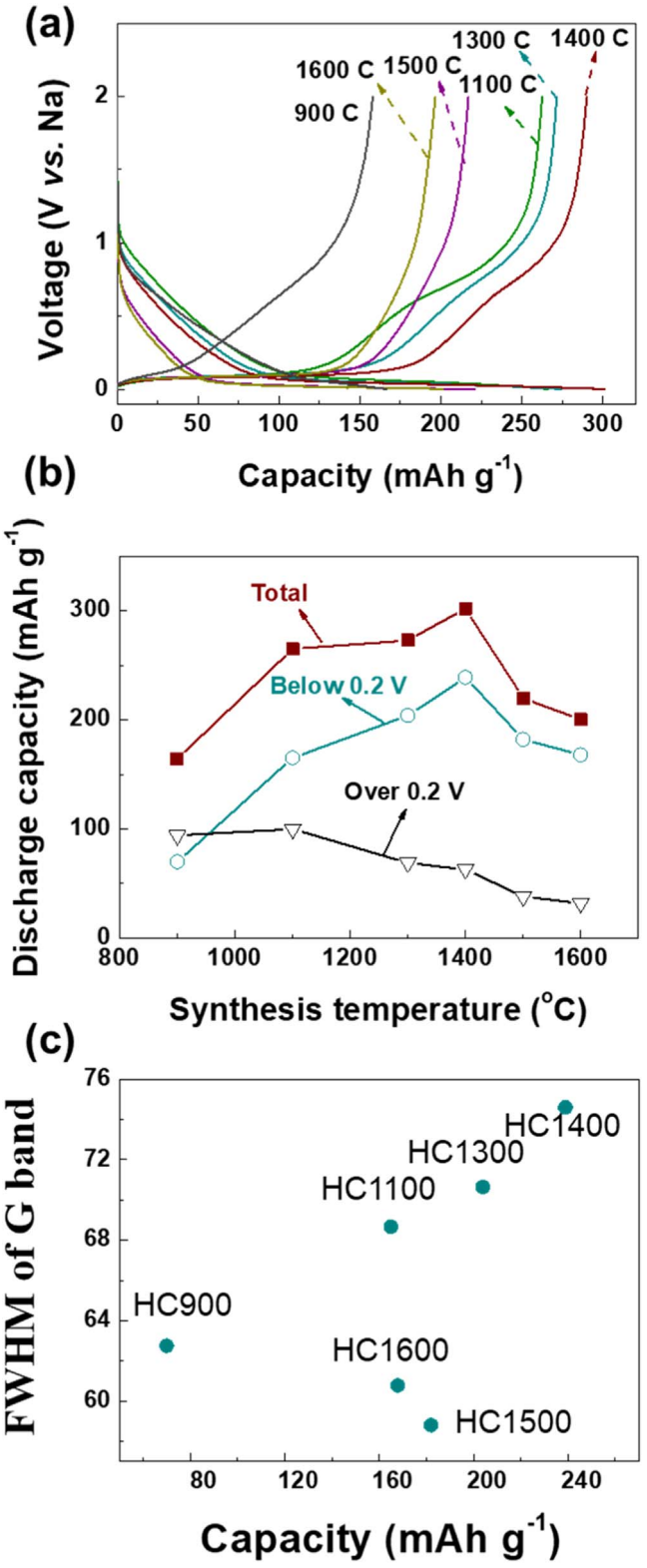

Figure 9. (a) Charge–discharge voltage profiles of HCs synthesized at varied temperatures in Na cells. (b) Synthesis temperatures vs discharge capacities. (c) Discharge capacity obtained below 0.2 V (plateau region) vs FWHM of the G band.

of the electrolyte on the particle surface with the formation of the SEI layer.[49] We find that the irreversible capacity decreases and the CE increases significantly when the synthesis temperature is higher than 1100 °C, as shown in Fig. 5b, which is highly likely related to the lower surface area confirmed by BET analysis. The maximum reversible capacity is obtained from the cellulose-derived HCs synthesized at 1100 °C. Figure 5c displays the cycling stability of the cellulose-derived HCs in Li cells. All the cellulose-derived HCs exhibit good cycling performance up to 40 cycles.

The Na-ion storage behavior of the cellulose-derived HCs was studied at a current rate of 15 mA g^{-1} in the voltage range of 0.001–2.0 V vs Na/Na^+, as shown in Fig. 6a. The cellulose-derived HCs show typical initial charge–discharge curves of HC electrodes, with a sloping voltage region above 0.2 V and a plateau region below 0.2 V vs Na/Na^+ (Fig. 6a).[50] The reversible/irreversible capacity of HC900, HC1100, HC1300, HC1400, HC1500, and HC1600 are 164/176, 265/109, 273/62, 286/99, 220/30, and 200/45 mAh g^{-1} with a CE of 48.2%, 70.9%, 81.5%, 74.3%, 88.0%, and 81.6%, respectively, for the first cycle. We expect that the irreversible capacity mainly originates from the electrolyte decomposition and SEI formation.[49] Figure 6b exhibits the reversible and irreversible capacities along with the CE as a function of the synthesis temperature. We find that the irreversible capacity decreases dramatically when the synthesis temperature increases, which is similar to the lithium storage behavior in HCs. The reversible capacity increases as the pyrolysis temperature rises, and the maximum reversible capacity is obtained from the cellulose-derived HCs synthesized at 1400 °C, which implies that the Na storage mechanisms could differ from the Li storage mechanisms. The cellulose-derived HCs synthesized at 1400 °C deliver the most stable cycle life among the samples tested, as illustrated in Fig. 6c.

We further tested the electrochemical potassium storage performance of the cellulose-derived HCs at a current rate of 15 mA g^{-1} in the voltage range of 0.001–2.0 V vs K/K^+. The cellulose-derived HCs deliver reversible/irreversible capacities of 52/125, 80/134, 57/94, 42/102, 25.8/117.2, and 22.5/116.5 mAh g^{-1} with a CE of 29.4%, 37.4%, 37.7%, 29.2%, 18.0%, and 16.2%, respectively, during the first charge and discharge process, as shown in Fig. 7a. We observed a much larger portion of irreversible capacity and much lower coulombic efficiency in the K cells than in the Li and Na cells. In addition, unlike for Li and Na cells, a significant decrease of the irreversible capacity was not observed at high synthesis temperature. In fact, the irreversible capacity was not noticeably affected by the synthesis temperature. These behaviors might indicate that the K electrolyte (1 M KPF_6 in EC/DEC) used in this study has a relatively low reduction stability. In fact, it was reported that carbonate-based K-electrolytes have relatively low reductive stability.[51,52] Figure 7b and Fig. 7c summarize the reversible and irreversible capacities and CE of the HC samples and their cycling stability, in which HC1100 shows the maximum reversible capacity, similar to the results from the Li cells.

Figure 8 summarizes the reversible capacities of the cellulose-derived HCs in Li, Na, and K cells as a function of the synthesis temperature. The Li and K storage capacities are maximized at 1100 °C and decrease at higher temperatures. In contrast, the reversible capacity for Na storage increases as the synthesis temperature increases up to 1400 °C and decreases at higher temperatures. This observation indicates that the optimized synthesis temperature of the cellulose-derived HCs can vary depending on the ion species being stored. We find that the reversible capacity decreases monotonically in Li and K cells above 1100 °C and that the charge–discharge curves have no noticeable plateaus, as demonstrated in Figs. 5a, 7a, and 8. Therefore, we expect that Li and K ions are mainly stored at the surface and/or defect sites of the cellulose-derived HCs. We suspect that lower K ion storage capacity in non-graphitic hard carbon than Li ion is attributable to the stronger electrostatic repulsion between K ions and/or steric effects due to larger ionic radius of K ion than Li ion. These can limit the total amount of adsorbed K ion on the non-graphitic hard carbon surface. However, we could not exclude the fact that the K-electrolyte is relatively less stable against K metal and at low voltages.[51,52] The significant electrolyte decomposition can lead to a large polarization of the cells, limiting reversible capacity. In contrast, the reversible capacity increases as the synthesis temperature

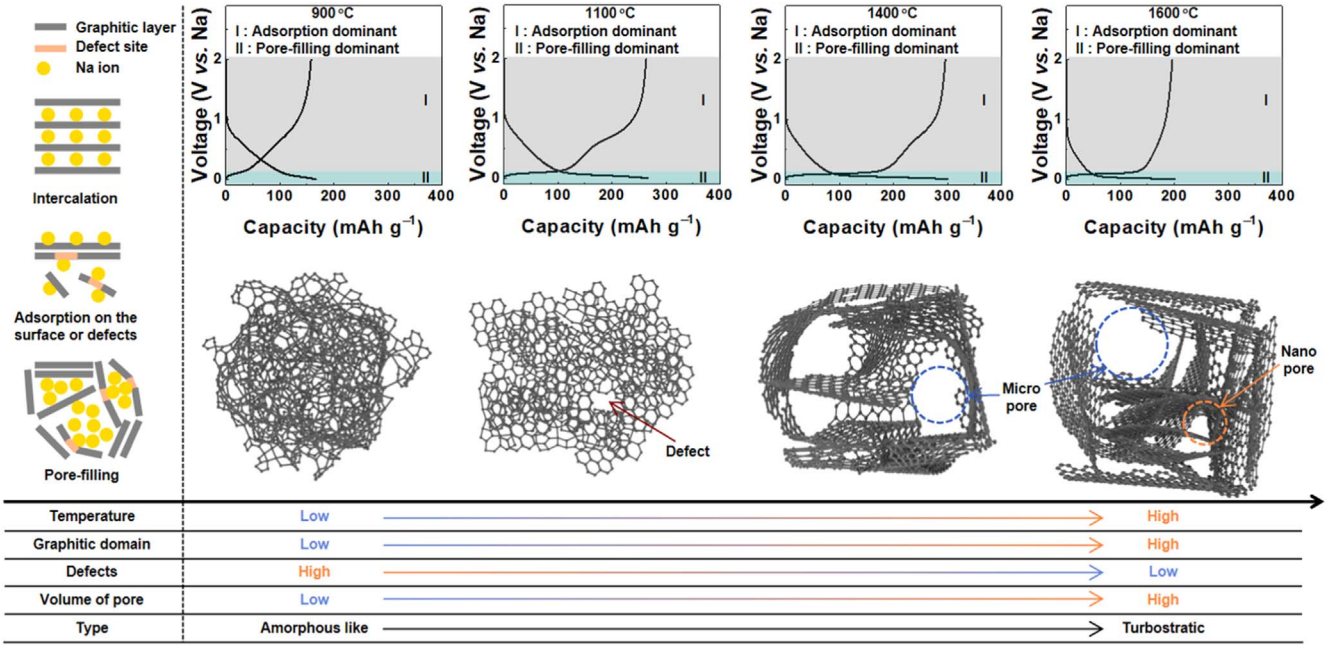

Figure 10. Schematic illustrations of sodium storage mechanisms and structural evolution depending on synthesis temperature.

increases from 900 °C to 1400 °C, and the highest reversible capacity is obtained from HC 1400 in Na cells. We also want to highlight that the charge–discharge profiles of Na cells are distinct from the Li and K cells. In Na cells, HCs exhibit plateaus in the low-voltage region (<0.2 V vs Na/Na^+), which are absent in Li and K cells. These results indicate that the Li and K storage mechanisms in HC might differ from that of Na in HC.

Understanding Na storage mechanisms in cellulose-derived HCs.—We plotted the second-cycle voltage profiles of cellulose-derived HCs in Na cells to capture how the Na storage behavior changes with the synthesis temperature, as shown in Fig. 9a. To more easily distinguish the capacity obtained from the sloped voltage region (>0.2 V) and plateau (<0.2 V), we put these discharge capacity values together obtained from cellulose-derived HCs, as shown in Fig. 9b. We find that the discharge capacity over 0.2 V (sloped voltage region) decreases as the synthesis temperature increases. More precisely, the discharge capacity in the high-voltage region is maximized at 1100 °C and decreases monotonically, which is identical to the results for Li and K cells. Therefore, we expect that the high-voltage region (>0.2 V) likely corresponds to the surface adsorption of Na ions and/or Na storage at defects. The cellulose used in this study has composition of $(C_6H_{10}O_5)_n$, indicating the HCs will have C and O only after the heat treatment. By the XPS analysis, we found that O-related functional groups are reduced at higher temperature process as shown in Fig. S3. It is well understood that O-related functional groups can take alkali ions at relatively high voltages by the adsorption mechanism.[53] Therefore, we expect that the O-containing functional groups contribute to the alkali ion adsorption/desorption at sloped voltage regions. As the synthesis temperature increases up to 1400 °C, the capacity obtained from the plateau region increases linearly but then decreases at higher temperatures. This behavior cannot be explained by the porosity increase observed in the SAXS results alone.

Interestingly, we find that the higher FWHM of the G band from the Raman spectra corresponds to a higher discharge capacity in the low-voltage plateau region, as shown in Fig. 9c. The capacity from the low-voltage region decreases above 1400 °C with decreasing FWHM of the G band, although the total volume of pore increases, as evident in the SAXS results (Fig. 1d). This finding might imply that the favorable sites for Na for the pore-filling mechanism are pores surrounded by curved carbon-sheet features.

Discussion

To investigate the sodium storage mechanisms in the cellulose-derived HCs and confirm the effect of the structural changes, as a function of the synthesis temperature, on the sodium storage mechanisms, the electrochemical properties and structural parameters that were characterized are summarized in Fig. 10. Based on our analysis above, we conclude that the cellulose-derived HCs have two dominant storage mechanisms: adsorption in region 1 and pore filling in region 2. The ratio of the capacities in region 1 and region 2 is directly related to the structure of the cellulose-derived HCs, as shown in Fig. 10. With the structural evolution from an amorphous-like to turbostratic structure, the graphitic domain and volume of pores increase while the defects decrease. The gradual decrease of the specific capacity in region 1 is attributed to the absorption site decrease with increasing degree of graphitization and decreasing defects and surface area, which is in agreement with the literature.[54] However, it is not possible to completely exclude the Na-insertion mechanism in the inter-slab distance between graphene sheets.[21,55] We expect that the pore-filling mechanism dominates the Na storage in the low-voltage region.[39,56] However, we find that the capacity obtained in the low-voltage region does not monotonically increase as the temperature increases, which agrees with previous reports.[20,25] Interestingly, the specific capacity in region 2 gradually increases until the synthesis temperature reaches 1400 °C and then decreases, which is attributed to the increase in the curve-featured pores up to 1400 °C and the decrease in the curve-featured pores above 1400 °C as confirmed by Raman analysis and TEM observations while the total pore volume increases monotonically as the temperature increases.[40] At temperatures above 1400 °C, we expect that the curved-featured carbon sheets are flattened and that less capacity is obtained in the plateau regions despite more pores being present. In our study, we could not find a linear correlation between interlayer space and Na storage capacity at low voltage plateau regions, which might exclude the Na intercalation mechanism at low voltage plateaus in our system. We suspect that the microstructure evolution of HCs is extremely sensitive to the synthesis processes and it can trigger distinct Na storage mechanisms, which requires further studies.

Conclusions

In this study, the structural evolution of cellulose-derived HCs prepared at various pyrolysis temperatures was characterized to understand the effects of the local structure, particularly the curved features, on the alkali-ion storage mechanisms using several physical, chemical, and electrochemical analytical techniques. We found that increasing the pyrolysis temperature results in two distinct effects on the non-graphitic HC structure. First, it leads to the development of graphitic basal planes and an increase in the orderness of the C–C bond angles. Second, it causes various forms of structural disordering such as the expansion of disordered carbon clusters, increased angle of edges, the formation of vacancies, and misalignment of layers until the temperature reaches 1400 °C. At temperatures above 1400 °C, the carbon structure becomes more ordered overall. These structural changes affect the ion-storage properties, and their effects depend on the alkali-ion species. HC 1100 delivered the highest reversible capacity in the case of Li and K ions, mainly due to the adsorption reactions. This finding indicates that Li and K ions are stored at the surface and/or in defects rather than in pores because HC 1100 shows a delicate balance between graphitic domain and defects but contains few pores. In the case of Na ions, it was revealed that the origin of the reversible capacity is the pore-filling mechanism in the low-voltage plateau region. Although HC 1400 contains fewer pores than HC 1500, HC 1400 with curve-featured pores displayed a higher reversible capacity than HC 1500. This result might indicate that curve-featured pores are the preferred Na-ion storage sites in the low-voltage plateau region. This work can be further used as a reference to develop efficient HCs for anodes in alkali-ion storage devices.

Acknowledgments

Work in the Molecular Foundry at LBNL was supported by the Office of Science, Office of Basic Energy Sciences, of the U.S. Department of Energy under contract no. DE-AC02–05CH11231. This work was supported by the National Research Foundation of Korea(NRF) grant funded by the Korea government(MSIT) (No. RS-2023–00249139). This research used resources of the Advanced Photon Source, a U.S. Department of Energy (DOE) Office of Science user facility operated for the DOE Office of Science by Argonne National Laboratory under Contract No. DE-AC02–06CH11357. This work was also supported by the Assistant Secretary for Energy Efficiency and Renewable Energy, Office of Vehicle Technologies of the US Department of Energy under Contract no. DE-AC02-05CH11231, under the Battery Materials Research Program directed by Tien Duong.

ORCID

Haeseong Jang https://orcid.org/0000-0002-1301-8627
Yoon Hwa https://orcid.org/0000-0002-3622-4837
Haegyeom Kim https://orcid.org/0000-0002-5962-8244

References

1. K. Ozawa, "Lithium-ion rechargeable batteries with LiCoO2 and carbon electrodes: the LiCoO2/C system." *Solid State Ionics*, **69**, 212 (1994).
2. H. Kim, H. Kim, Z. Ding, M. H. Lee, K. Lim, G. Yoon, and K. Kang, "Recent progress in electrode materials for sodium-ion batteries." *Adv. Energy Mater.*, **6**, 1600943 (2016).
3. Z. Jian, Z. Xing, C. Bommier, Z. Li, and X. Ji, "Hard carbon microspheres: potassium-ion anode versus sodium-ion anode." *Adv. Energy Mater.*, **6**, 1501874 (2016).
4. M. Chen, Q. Liu, Y. Zhang, G. Xing, S.-L. Chou, and Y. Tang, "Emerging polyanionic and organic compounds for high energy density, non-aqueous potassium-ion batteries." *J. Mater. Chem. A*, **8**, 16061 (2020).
5. Y. Qi, L. Mu, J. Zhao, Y.-S. Hu, H. Liu, and S. Dai, "Superior Na-Storage performance of low-temperature-synthesized Na3(VO1−xPO4)2F1+2x (0⩽x⩽1) nanoparticles for Na-Ion batteries." *Angew. Chem. Int. Ed.*, **54**, 9911 (2015).
6. Q. Zhang, Z. Wang, S. Zhang, T. Zhou, J. Mao, and Z. Guo, "Cathode materials for potassium-ion batteries: current status and perspective." *Electrochemical Energy Reviews*, **1**, 625 (2018).
7. S. Xu et al., "Fe-Based Tunnel-Type Na0.61[Mn0.27Fe0.34Ti0.39]O2 designed by a new strategy as a cathode material for sodium-ion batteries." *Adv. Energy Mater.*, **5**, 1501156 (2015).
8. Y. Wang, R. Xiao, Y.-S. Hu, M. Avdeev, and L. Chen, "P2-Na0.6[Cr0.6Ti0.4]O2 cation-disordered electrode for high-rate symmetric rechargeable sodium-ion batteries." *Nat. Commun.*, **6**, 6954 (2015).
9. A. P. Cohn, N. Muralidharan, R. Carter, K. Share, L. Oakes, and C. L. Pint, "Durable potassium ion battery electrodes from high-rate cointercalation into graphitic carbons." *J. Mater. Chem. A*, **4**, 14954 (2016).
10. X. Zhang, S. Han, C. Fan, L. Li, and W. Zhang, "Hard carbon enveloped with graphene networks as lithium ion battery anode." *Mater. Lett.*, **138**, 259 (2015).
11. J. Ding, H. Zhang, H. Zhou, J. Feng, X. Zheng, C. Zhong, E. Paek, W. Hu, and D. Mitlin, "Sulfur-grafted hollow carbon spheres for potassium-ion battery anodes." *Adv. Mater.*, **31**, 1900429 (2019).
12. A. Metrot, D. Guerard, D. Billaud, and A. Herold, "New results about the sodium-graphite system." *Synth. Met.*, **1**, 363 (1980).
13. R. C. Asher and S. A. Wilson, "Lamellar compound of sodium with graphite." *Nature*, **181**, 409 (1958).
14. H. Lei, J. Li, X. Zhang, L. Ma, Z. Ji, Z. Wang, L. Pan, S. Tan, and W. Mai, "A review of hard carbon anode: rational design and advanced characterization in potassium ion batteries." *InfoMat*, **4**, e12272 (2022).
15. S. M. Mamun, T. Kamiyama, and M. Nagao, *Effect of Lithium Intercalation On The Structure of Non-Graphitizable Carbon: Small-Angle Neutron Scattering* (Physical Society of Japan, Tokyo, Japan) (2001).
16. T. Zheng, Q. Zhong, and J. R. Dahn, "High-capacity carbons prepared from phenolic resin for anodes of lithium-ion batteries." *J. Electrochem. Soc.*, **142**, L211 (1995).
17. D. A. Stevens and J. R. Dahn, "High capacity anode materials for rechargeable sodium-ion batteries." *J. Electrochem. Soc.*, **147**, 1271 (2000).
18. K. Kubota et al., "Structural analysis of sucrose-derived hard carbon and correlation with the electrochemical properties for lithium, sodium, and potassium insertion." *Chem. Mater.*, **32**, 2961 (2020).
19. Nagmani, A. Tyagi, and S. Puravankara, "Insights into the diverse precursor-based micro-spherical hard carbons as anode materials for sodium–ion and potassium–ion batteries." *Materials Advances*, **3**, 810 (2022).
20. H. Au et al., "A revised mechanistic model for sodium insertion in hard carbons." *Energy Environ. Sci.*, **13**, 3469 (2020).
21. M. Anji Reddy, M. Helen, A. Groß, M. Fichtner, and H. Euchner, "Insight into sodium insertion and the storage mechanism in hard carbon." *ACS Energy Lett.*, **3**, 2851 (2018).
22. C. Zhao, Q. Wang, Y. Lu, B. Li, L. Chen, and Y.-S. Hu, "High-temperature treatment induced carbon anode with ultrahigh Na storage capacity at low-voltage plateau." *Sci. Bull.*, **63**, 1125 (2018).
23. Y. Lu, C. Zhao, X. Qi, Y. Qi, H. Li, X. Huang, L. Chen, and Y.-S. Hu, "Pre-oxidation-tuned microstructures of carbon anodes derived from pitch for enhancing Na storage performance." *Adv. Energy Mater.*, **8**, 1800108 (2018).
24. Q. Meng, Y. Lu, F. Ding, Q. Zhang, L. Chen, and Y.-S. Hu, "Tuning the closed pore structure of hard carbons with the highest Na storage capacity." *ACS Energy Lett.*, **4**, 2608 (2019).
25. A. Gomez-Martin, J. Martinez-Fernandez, M. Ruttert, M. Winter, T. Placke, and J. Ramirez-Rico, "Correlation of Structure and Performance of Hard Carbons as Anodes for Sodium Ion Batteries." *Chem. Mater.*, **31**, 7288 (2019).
26. A. M. Escamilla-Pérez, A. Beda, L. Simonin, M.-L. Grapotte, J. M. Le-Meins, and C. Matei Ghimbeu, "Biopolymer-based hard carbons: correlations between properties and performance as a na-ion battery anode." *ACS Appl. Energy Mater.*, **6**, 7419 (2023).
27. H. Yamamoto, S. Muratsubaki, K. Kubota, M. Fukunishi, H. Watanabe, J. Kim, and S. Komaba, "Synthesizing higher-capacity hard-carbons from cellulose for Na- and K-ion batteries." *J. Mater. Chem. A*, **6**, 16844 (2018).
28. S. Komaba, W. Murata, T. Ishikawa, N. Yabuuchi, T. Ozeki, T. Nakayama, A. Ogata, K. Gotoh, and K. Fujiwara, "Electrochemical Na insertion and solid electrolyte interphase for hard-carbon electrodes and application to na-ion batteries." *Adv. Funct. Mater.*, **21**, 3859 (2011).
29. V. Simone, A. Boulineau, A. de Geyer, D. Rouchon, L. Simonin, and S. Martinet, "Hard carbon derived from cellulose as anode for sodium ion batteries: Dependence of electrochemical properties on structure." *Journal of Energy Chemistry*, **25**, 761 (2016).
30. D. A. Stevens and J. R. Dahn, "The mechanisms of lithium and sodium insertion in carbon materials." *J. Electrochem. Soc.*, **148**, A803 (2001).
31. N. Shimodaira and A. Masui, "Raman spectroscopic investigations of activated carbon materials." *J. Appl. Phys.*, **92**, 902 (2002).
32. A. Sadezky, H. Muckenhuber, H. Grothe, R. Niessner, and U. Pöschl, "Raman microspectroscopy of soot and related carbonaceous materials: Spectral analysis and structural information." *Carbon*, **43**, 1731 (2005).
33. A. C. Ferrari and D. M. Basko, "Raman spectroscopy as a versatile tool for studying the properties of graphene." *Nat. Nanotechnol.*, **8**, 235 (2013).
34. J. D. Herdman, B. C. Connelly, M. D. Smooke, M. B. Long, and J. H. Miller, "A comparison of Raman signatures and laser-induced incandescence with direct numerical simulation of soot growth in non-premixed ethylene/air flames." *Carbon*, **49**, 5298 (2011).
35. L. Bokobza, J.-L. Bruneel, and M. Couzi, "Raman spectra of carbon-based materials (from Graphite to Carbon Black) and of some silicone composites." *C*, **1**, 77 (2015).
36. H. Moon, M. Zarrabeitia, E. Frank, O. Böse, M. Enterría, D. Saurel, I. Hasa, and S. Passerini, "Assessing the reactivity of hard carbon anodes: linking material

properties with electrochemical response upon sodium- and lithium-ion storage." *Batteries & Supercaps*, **4**, 960 (2021).
37. A. Cuesta, P. Dhamelincourt, J. Laureyns, A. Martínez-Alonso, and J. M. D. Tascón, "Raman microprobe studies on carbon materials." *Carbon*, **32**, 1523 (1994).
38. A. C. Ferrari, "A model to interpret the raman spectra of disordered, amorphous and nanostructured carbons." *MRS Online Proceedings Library*, **675**, 1151 (2011).
39. V. L. Deringer, C. Merlet, Y. Hu, T. H. Lee, J. A. Kattirtzi, O. Pecher, G. Csányi, S. R. Elliott, and C. P. Grey, "Towards an atomistic understanding of disordered carbon electrode materials." *Chem. Commun.*, **54**, 5988 (2018).
40. K. Jurkiewicz, M. Pawlyta, D. Zygadło, D. Chrobak, S. Duber, R. Wrzalik, A. Ratuszna, and A. Burian, "Evolution of glassy carbon under heat treatment: correlation structure–mechanical properties." *J. Mater. Sci.*, **53**, 3509 (2018).
41. T. K. Kumaresan, S. A. Masilamani, K. Raman, S. Z. Karazhanov, and R. Subashchandrabose, "High performance sodium-ion battery anode using biomass derived hard carbon with engineered defective sites." *Electrochim. Acta*, **368**, 137574 (2021).
42. J. Jiang, R. Pachter, F. Mehmood, A. E. Islam, B. Maruyama, and J. J. Boeckl, "A Raman spectroscopy signature for characterizing defective single-layer graphene: Defect-induced I(D)/I(D') intensity ratio by theoretical analysis." *Carbon*, **90**, 53 (2015).
43. C. Casiraghi, A. Hartschuh, H. Qian, S. Piscanec, C. Georgi, A. Fasoli, K. S. Novoselov, D. M. Basko, and A. C. Ferrari, "Raman spectroscopy of graphene edges." *Nano Lett.*, **9**, 1433 (2009).
44. A. C. Ferrari et al., "Raman spectrum of graphene and graphene layers." *Phys. Rev. Lett.*, **97**, 187401 (2006).
45. C. H. Lui, Z. Li, Z. Chen, P. V. Klimov, L. E. Brus, and T. F. Heinz, "Imaging stacking order in few-layer graphene." *Nano Lett.*, **11**, 164 (2011).
46. K. Kim, S. Coh, L. Z. Tan, W. Regan, J. M. Yuk, E. Chatterjee, M. F. Crommie, M. L. Cohen, S. G. Louie, and A. Zettl, "Raman spectroscopy study of rotated double-layer graphene: misorientation-angle dependence of electronic structure." *Phys. Rev. Lett.*, **108**, 246103 (2012).
47. A. C. Ferrari and J. Robertson, "Interpretation of Raman spectra of disordered and amorphous carbon." *Physical Review B*, **61**, 14095 (2000).
48. J. Yang, X.-y. Zhou, J. Li, Y.-l. Zou, and J.-j. Tang, "Study of nano-porous hard carbons as anode materials for lithium ion batteries." *Mater. Chem. Phys.*, **135**, 445 (2012).
49. A. Kamiyama, K. Kubota, D. Igarashi, Y. Youn, Y. Tateyama, H. Ando, K. Gotoh, and S. Komaba, "MgO-Template synthesis of extremely high capacity hard carbon for Na-Ion battery." *Angew. Chem. Int. Ed.*, **60**, 5114 (2021).
50. N. Yabuuchi, K. Kubota, M. Dahbi, and S. Komaba, "Research development on sodium-ion batteries." *Chem. Rev.*, **114**, 11636 (2014).
51. T. Hosaka, S. Muratsubaki, K. Kubota, H. Onuma, and S. Komaba, "Potassium metal as reliable reference electrodes of nonaqueous potassium cells." *J. Phys. Chem. Letters*, **10**, 3296 (2019).
52. L. Caracciolo, L. Madec, G. Gachot, and H. Martinez, "Impact of the salt anion on K metal reactivity in EC/DEC studied using GC and XPS analysis." *ACS Appl. Mater. Interfaces*, **13**, 57505 (2021).
53. T. Xu, X. Qiu, X. Zhang, and Y. Xia, "Regulation of surface oxygen functional groups and pore structure of bamboo-derived hard carbon for enhanced sodium storage performance." *Chem. Eng. J.*, **452**, 139514 (2023).
54. P. Bai, Y. He, X. Zou, X. Zhao, P. Xiong, and Y. Xu, "Elucidation of the Sodium-storage mechanism in hard carbons." *Adv. Energy Mater.*, **8**, 1703217 (2018).
55. H. Alptekin, H. Au, A. C. S. Jensen, E. Olsson, M. Goktas, T. F. Headen, P. Adelhelm, Q. Cai, A. J. Drew, and M.-M. Titirici, "Sodium storage mechanism investigations through structural changes in hard carbons." *ACS Appl. Energy Mater.*, **3**, 9918 (2020).
56. J. M. Stratford, P. K. Allan, O. Pecher, P. A. Chater, and C. P. Grey, "Mechanistic insights into sodium storage in hard carbon anodes using local structure probes." *Chem. Commun.*, **52**, 12430 (2016).